Improving Space Object Catalog Maintenance Through Advances in Solar Radiation Pressure Modeling

Jay McMahon
University of Colorado Boulder
Daniel J. Scheeres
University of Colorado Boulder

Abstract

This paper investigates the weaknesses of using the cannonball model to represent the solar radiation pressure force on an object in an orbit determination process, and presents a number of alternative models that greatly improve the orbit determination performance. These weaknesses are rooted in the fact that the cannonball model is not a good representation of the true solar radiation pressure force acting on an arbitrary object. Using an erroneous force model results in poor estimates, inaccurate trajectory propagation, unrealistic covariances, and the inability to fit long and/or dense arcs of data. The alternative models presented are derived from a Fourier series representation of the solar radiation pressure force. The simplest instantiation of this model requires only two more parameters to be estimated, however this results in orders of magnitude improvements in tracking accuracy. This improvement is illustrated through numerical examples of a discarded upper stage in a geosynchronous transfer orbit, and more drastically for a piece of high area-to-mass ratio debris in a near-geosynchronous orbit. Implementation of improved solar radiation pressure models in this manner will alleviate track correlation, object identification, and sensor tasking issues that plague current catalog maintenance due to the standard inaccurate dynamic model.

1 Introduction

Solar radiation pressure (SRP) forces are the largest non-gravitational perturbation forces at altitudes above low-Earth orbit. These forces are especially important for objects with high area-to-mass ratios (HAMR) [1, 2, 29], and are therefore of great interest in studies of orbital debris since there are many HAMR objects in this group. This dependence on the area-to-mass ratio has been studied by several authors [6, 8, 28, 27], who all find this to be an important factor in the evolution of the debris' orbits. The study of this effect is typically made by using a constant force model with zero torques [7, 8, 1, 26], known as the cannonball model. However, it has been shown [12, 20, 21, 22] that improvement in the predicted evolution can be made in many cases by using a more detailed model.

Precise orbit determination requires, by definition, force models for the filter dynamic model that closely represent reality. High-fidelity SRP models have been used to this end for many satellites including ICEsat [15], Topex/Poseiden [14], GPS [16, 17, 18, 13], and GRACE [10] to name a few. Unfortunately, the very precise orbit determination results obtained for LAGEOS using the cannonball model [11] convinced many people that the cannonball model was all that was necessary for an SRP model. The problem is that LAGEOS *was a cannonball*, so that model was quite accurate for that particular satellite!

The purpose of this paper is to illustrate the shortcomings of using the cannonball SRP model for orbit determination and to present alternative SRP models that do not have these weaknesses. These improved SRP models could greatly improve catalog maintenance issues over the status quo, as discussed in Ref. [19]. An accurate force model allows for precise orbit determination with realistic covariance bounds, and most importantly allows these estimates to be propagated such that the covariance envelope realistically contains the object in the future. This is a necessity for proper track correlation and object identification, which both depend on accurate propagation and covariance realism. Furthermore, using a more realistic force model will reduce sensor tasking issues with current tracking networks. Sensing resources are being wasted to track even large objects because more regular tracking must be used to make up for the fact that the cannonball based predictions are only useful for short periods of time. Similarly, an improved force model allows longer and more dense arcs of data to be used to maintain catalog entries. This will increase the information associated with these entries since old data will not need to be discarded in order to fit the data. There are

significant efforts underway to improve the amount and accuracy of data for orbital objects, however if the dynamical modeling is not improved along with the tracking infrastructure, the improvement in the accuracy and amount of data collected will be for naught.

The paper is organized as follows. First, a background on SRP modeling is provided, and the suggested models needed for orbit determination are given. The crux of the paper is Section 3, where the numerical examples illustrate the improved performance that is achieved with improved SRP models over the cannonball model. Finally conclusions and next steps are discussed in 4.

2 Solar Radiation Pressure Modeling

In general, the incoming radiation pressure from the Sun exerts a force (and generally a torque) on any body it intersects. This force depends on the shape of the body and the optical properties of the body that govern how light is reflected and absorbed as it intersects the surface. The SRP force produced at any time is determined by integrating the exchange of momentum over the surface area of the body that are illuminated by the Sun, which is in direction $\hat{\mathbf{u}}$ from the body, as well as those areas that are not directly illuminated by the Sun, but receive energy as it is re-emitted and/or reflected from Sun-lit portions of the body. In order to make these computations tractable, the body of interest is sub-divided into a finite number of differential areas, termed facets, that are planar and usually triangular. The SRP force is then determined as

$$\mathbf{F}_{SRP} = \Phi \frac{G_1}{R^2} \sum_{i=1}^{N} \mathbf{f}_i(\hat{\mathbf{u}}) \tag{1}$$

where N is the number of surface elements used to describe the body, $\mathbf{f}_i$ is a generalized area (units of km^2) for each facet that encompasses the physics of the SRP-surface interaction, G_1 is the solar radiation constant and is equal to 1×10^{14}kg km/s^2, and R is the distance from the Sun (in units km). Φ is the Sun shadow factor, that is set to zero when the body is shadowed by the Earth, thus turning off the SRP force. Although this is an important factor to consider for accurate dynamical predictions (e.g. Ref. [30]), this factor is ignored in this paper for simplicity.

There are many different models for the reflection of light that can be used to compute $\mathbf{f}_i$. These models are called bidirectional reflectance distribution functions (BRDFs); the most widely used are the Lambertian[4, 5, 3, 23, 9, 21], Ashikhmin-Shirley[24], and Cook-Torrance[25]. Regardless of the specific model chosen, the BRDF takes the shape and optical properties of the body in question, and for a given $\hat{\mathbf{u}}$, the BRDF computes the amount of light reflected in any particular direction. Integrating over all reflection directions, the total momentum exchange from the incoming sunlight can be determined. Therefore the produced force varies as the body changes its orientation with respect to the Sun, and thus $\hat{\mathbf{u}}$ changes when expressed in the body-fixed frame. In general this force will be predominantly in the direction away from the Sun, but not purely aligned in that direction.

In this study, the classical Lambertian BRDF is used to compute the true SRP force for a given object. This model shows that for a given surface, there is a component of the force in the surface normal direction, and a component in the plane of the surface in the opposite direction of the Sun. The generalized area for each facet for a given position of the Sun is computed as[3]

$$\mathbf{f}_i = -\left[\left\{ \rho_i s_i \left(2\hat{\mathbf{n}}_i\hat{\mathbf{n}}_i - \bar{\bar{U}} \right) + \bar{\bar{U}} \right\} \cdot \hat{\mathbf{u}}\hat{\mathbf{u}} \cdot \hat{\mathbf{n}}_i + a_{2i}\hat{\mathbf{n}}_i\hat{\mathbf{n}}_i \cdot \hat{\mathbf{u}} \right] H_i(\hat{\mathbf{u}}) A_i \tag{2}$$

with

$$a_{2i} = B(1 - s_i)\rho_i + (1 - \rho_i)B \tag{3}$$

where i is an index that identifies each surface element of the satellite. Each surface has a normal unit vector, $\hat{\mathbf{n}}_i$, a surface area, A_i, a total reflectivity, ρ_i, and the specular fraction of the reflectivity, s_i. B is the Lambertian scattering coefficient of the surface (ideally equal to 2/3 [9]), $\hat{\mathbf{u}}$ is the Sun unit vector from the surface element to the Sun, and $\bar{\bar{U}}$ is the identity dyad. $H(\hat{\mathbf{u}})$ is the visibility function which captures the effects of both the local facet horizon and shadowing from other portions of the body. If the facet is not illuminated by the Sun at this orientation, $H(\hat{\mathbf{u}}) = 0$; if the entire facet is illuminated by the Sun, $H(\hat{\mathbf{u}}) = 1$; otherwise, if part of the facet is shadowed by other portions of the body, $0 < H(\hat{\mathbf{u}}) < 1$.

In reality, the only way to determine the true BRDF for all of the different materials used on spacecraft and launch vehicles that end up in Earth orbit is through lab testing. However, even if materials are perfectly characterized on

Earth, their optical properties, and thus the BRDF and resulting SRP forces, will change once the material spends time exposed to the harshness of space. Therefore, even using a ground-based BRDF will generally require additional estimation. In this paper, the Lambertian model is chosen for its simplicity and ease of understanding. The results presented in this paper are not strongly sensitive to the particular SRP model, and using the Ashikhmin-Shirley or Cook-Torrance models would give qualitatively similar results for the study presented here due to the fact that they will have acceleration components in directions other than $-\hat{\mathbf{u}}$ which the cannonball model doesn't capture.

Regardless of any modeling issues, the SRP force is fundamentally dependent on $\hat{\mathbf{u}}$. One physically meaningful way of expressing this interaction is from a body-fixed frame, where the location of the Sun with respect to the body can be expressed as

$$\hat{\mathbf{u}} = \cos\delta_s \cos\lambda_s \hat{\mathbf{x}}_b + \cos\delta_s \sin\lambda_s \hat{\mathbf{y}}_b + \sin\delta_s \hat{\mathbf{z}}_b \tag{4}$$

where δ_s is the Sun's latitude, and λ_s is the Sun's longitude with respect to this body-fixed frame. Thus, the SRP acceleration can be expressed for any location of the Sun in the body-fixed frame as in McMahon and Scheeres [5, 3]

$$\mathbf{a}_{SRP} = \frac{G_1}{mR^2} \sum_{n=0}^{\infty} [\mathbf{A}_n(\delta_s)\cos(n\lambda_s) + \mathbf{B}_n(\delta_s)\sin(n\lambda_s)] \tag{5}$$

by fitting the computed SRP acceleration (based on any model) as a set of Fourier series in the body-fixed frame. For the case when the object spin vector is aligned with its orbit angular momentum, it has been shown that only seven of these coefficients are necessary to understand the secular evolution of any object in circular orbit, while other coefficients appear as a power series with eccentricity for non-circular orbits. Even in the case when the spin vector is not strictly aligned with the angular momentum, but its motion is periodic with the orbit period, these results will hold. [4, 13] Furthermore, although not addressed explicitly in this work, the Fourier coefficients can also encompass the effect of the Sun shadow factor, Φ, as was shown in Ref. [4]. Therefore using a Fourier series representation such as this is a powerful way to compress the perturbative effect of SRP into a finite number of parameters.

The Fourier model representation of the SRP acceleration has many advantages for estimation - the coefficients are orthogonal by design and the main perturbative effects are captured in a finite number of parameters as discussed previously. However, the most important benefit from using this model is that none of the shape or material information needed to use a BRDF has to be explicitly known or estimated; all of this information is wrapped up into the Fourier coefficients. The perturbation is then directly represented based on the observations of the object in orbit without needing to derive or compute the BRDF.

The SRP acceleration is generalized for estimation problems from Eq. (5) in terms of an object's spin rate as

$$\begin{aligned} {}^I\mathbf{a}_{SRP} = \frac{G_1}{mR^2} \sum_{n=0}^{\infty} & \left[{}^I\hat{\mathbf{e}}_1 {}^E\mathbf{A}_n^{(1)} + {}^I\hat{\mathbf{e}}_2 {}^E\mathbf{A}_n^{(2)} + {}^I\hat{\mathbf{e}}_3 {}^E\mathbf{A}_n^{(3)} \right] \cos(n\omega t) \\ & + \left[{}^I\hat{\mathbf{e}}_1 {}^E\mathbf{B}_n^{(1)} + {}^I\hat{\mathbf{e}}_2 {}^E\mathbf{B}_n^{(2)} + {}^I\hat{\mathbf{e}}_3 {}^E\mathbf{B}_n^{(3)} \right] \sin(n\omega t) \end{aligned} \tag{6}$$

where ω is the spin rate of the object, and t is the time since epoch. The superscript E signifies that the coefficient vectors are described in some frame for which the basis is $\hat{\mathbf{e}}_1$, $\hat{\mathbf{e}}_2$, $\hat{\mathbf{e}}_3$. These vectors are expressed in the same frame as the desired SRP acceleration, signified by the superscript I. The (1), (2), or (3) superscripts indicates the component of the coefficient vector expressed in the E-frame. This formulation allows the acceleration vector to be expressed in some preferred frame, but the SRP coefficient vectors to be derived in a different frame. For example, in the typical application the SRP acceleration will be expressed in the Earth-centered inertial frame (ECI) and the coefficients will be expressed in some body-fixed frame. If the body-fixed frame is unknown, the local-vertical local-horizontal (LVLH) frame can also be used [4]. For the remainder of the document, the I and E super-scripts are dropped but are inferred by the presence of the basis vectors.

The following sub-sections discuss the most common uses of the SRP model for orbit determination in terms of the general Fourier model presented above. The different versions of the model depend upon the attitude dynamics of the object in question. Further details of these models, including necessary partials, are derived in [32].

2.1 Cannonball Model

The most commonly used simplified SRP model is known as the cannonball model [11]. This model represents the SRP force as a constant magnitude force acting directly away from the Sun, and is typically expressed as

$$\mathbf{a}_{SRP} = -C_R \frac{G_1}{R^2} \frac{A}{m} \hat{\mathbf{u}} \tag{7}$$

where C_R is the coefficient that scales the body reflectivity, and for a body with constant optical properties is

$$C_R = 1 + \rho \tag{8}$$

Effectively, this model assumes that the object is a sphere with uniform optical properties because the area that intersects the sunlight is the same from any direction and the force is directed entirely away from the Sun, which only happens if the optical properties are identical around the surface of the sphere.

For most objects, these assumptions are incorrect. However, it has been shown in the past [26, 7] that the cannonball model can effectively represent the average SRP force on an object if that object is tumbling freely such that at any time there is an equal probability of any attitude orientation with respect to the Sun. If the tumbling rates are much faster than the orbital rates, this averaged SRP force could be adequate for orbit determination, especially for objects with low area-to-mass ratios.

2.2 3-constant Model

The classical cannonball model is limited by design to act in only one direction, directly away from the Sun. However, for any realistic object the SRP force will be 3-dimensional in nature. Furthermore, previous studies have shown that the averaged SRP force on HAMR objects integrated with 6 degree-of-freedom dynamics does not approach the cannonball model because the attitude motion does not meet the definition of tumbling used in the previous section[12]. Therefore, the model presented here is effectively a 3-dimensional version of the cannonball model.

In this case, the preferred frame for the SRP acceleration is a rotating frame tied to the Earth's heliocentric orbit, defined by basis vectors $\hat{\mathbf{U}}$, $\hat{\mathbf{V}}$, and $\hat{\mathbf{W}}$ (referred to as the UVW frame later). The basis vectors are defined as follows,

$$\hat{\mathbf{U}} = -\frac{\mathbf{R_E}}{R_E} \tag{9}$$

$$\hat{\mathbf{W}} = \cos(\phi)\hat{\mathbf{Z}}_I - \sin(\phi)\left(\hat{\mathbf{Z}}_I \times \hat{\mathbf{U}}\right) \tag{10}$$

$$\hat{\mathbf{V}} = \hat{\mathbf{W}} \times \hat{\mathbf{U}} \tag{11}$$

where ϕ is the obliquity of the Earth's spin axis (approximately $23.4°$) and $\hat{\mathbf{Z}}_I$ is the direction of the Earth's heliocentric orbit angular momentum vector. Note that in this case the choice of $\hat{\mathbf{V}}$ and $\hat{\mathbf{W}}$ are not crucial, as long as they are used consistently. The definition of $\hat{\mathbf{U}}$, however, is very important, as discussed below.

The SRP acceleration is then defined as,

$$\mathbf{a}_{SRP} = \frac{G_1}{mR^2}\left[{}^I\hat{\mathbf{U}}\mathbf{A}_0^{(1)} + {}^I\hat{\mathbf{V}}\mathbf{A}_0^{(2)} + {}^I\hat{\mathbf{W}}\mathbf{A}_0^{(3)}\right] \tag{12}$$

The idea with this formulation is that it is a generalization of the commonly used cannonball model, which can be defined from Eq. (12) with $\mathbf{A}_0^{(2)} = \mathbf{A}_0^{(3)} = 0$ and $\mathbf{A}_0^{(1)} = C_R A$ being the usually estimated SRP scale factor. Note that this coefficient will be negative in this case since $\hat{\mathbf{U}}$ points towards the Sun. Technically since $\hat{\mathbf{U}}$ is defined to point from the Earth to the Sun instead of the object to the Sun, there is a small difference in direction here as well. However, most implementations of the cannonball model assume no difference between the $\hat{\mathbf{U}}$ from the Earth vs $\hat{\mathbf{u}}$ from an orbiting object since even in GEO, this difference only reaches approximately 2.8×10^{-4} radians. In the 3-constant model presented here, however, there are also terms that provide an acceleration perpendicular to the $\hat{\mathbf{U}}$ direction, which generally makes this model able to capture a wider array of perturbing effects from SRP.

The basis vectors, as shown above, depend only on the motion of the Earth about the Sun. As such, these are taken as known parameters. In this case, there is no state-dependent angular velocity to consider for estimation.

2.3 Inertially Fixed Uniform Rotator

In this case, the preferred frame for the SRP acceleration is an inertially fixed frame with the $\hat{\mathbf{e}}_3$ basis vector being taken as the spin axis of the object. The other two basis vectors can be defined in any consistent manner. The basis vectors are considered constant and known. This case is motivated by debris objects with known, stable spin vectors (i.e. negligible change due to external torques over the data arc). This would include objects such as defunct satellites or upper stages that are in a minimum energy principle axis rotation state.

The basis vectors for this case are chosen such that one of the basis directions aligns with the spin direction, and the other two are just made perpendicular. Thus, these basis vectors do not depend on the object's translational state.In this case, ω is a constant that does not depend on $\mathbf{r}$ or $\mathbf{v}$, but the angular velocity could be estimated.However due to the dependence of t in those relationships, estimating the spin rate can be difficult for long arcs of data, and thus may not be recommended. In practice, it is recommend to estimate with a fixed value for ω over shorter sub-arcs. If over subsequent arcs the estimated values of the coefficients seem to be drifting, this may be an indication that ω should be estimated, and the previously estimated values of the coefficients should then give a good starting point.

2.4 Object Uniformly Rotates with the Orbit

This case is motivated by the many satellites or objects that are in synchronous orbits with one side always facing the Earth. This resonance between the attitude and orbital motion gives rise to many secular effects from the SRP force, which are discussed in detail in Refs. [5] and [4]. An example of precise orbit determination with this model was presented in Ref. [13], however the partials were not presented, and are given here for completeness.

In this case, the preferred frame is the LVLH frame associated with the object. The basis vectors are $\hat{\mathbf{e}}_1 = \hat{\mathbf{r}}$, which is the radial direction, $\hat{\mathbf{e}}_3 = \hat{\mathbf{h}}$ is the out-of-plane direction along the orbit's angular momentum vectors, and $\hat{\mathbf{e}}_2 = \hat{\mathbf{s}} = \hat{\mathbf{h}} \times \hat{\mathbf{r}}$. The angular velocity is defined as the Keplerian true anomaly rate. Unlike the previous cases, the definitions of the basis vectors as the LVLH frame and the angular velocity as the orbit rate gives rise to dependence on the position and velocity vectors.

As mentioned above, the angular velocity is defined as the Keplerian orbit rate

$$\omega = \dot{\nu} = \frac{h}{r^2} \tag{13}$$

where ν is the true anomaly.

3 Numerical Examples

In this section, two test cases are presented to illustrate the effects of mis-modeling SRP for the estimation and propagation of common debris populations. The first example is a defunct launch vehicle upper stage, spinning freely in a geosynchronous transfer orbit (GTO), and the second case is a high area-to-mass-ratio (HAMR) object in geosynchronous orbit (GEO). Not only are these representative debris objects, but they also represent the extreme cases of the expected effects of SRP based on the disparities in their AMRs. In both cases, it has been argued in the past that the cannonball model is sufficient for the SRP perturbation; for the low AMR objects because the cannonball model captures the main effect of a small perturbation and the other components are too small to matter, and for the HAMR objects because they will be in a tumbling motion the SRP effects could be averaged to the cannonball model [7]. We show here that these assumptions are not proper.

In order to plainly illustrate the effects of the SRP model, the dynamics are kept fairly simple so that the only forces considered in these simulations are a 12x12 Earth gravity field and SRP. The true SRP model used to simulate the date in these examples is computed by an order 25 Fourier series computed from a Lambertian SRP model based on the shape models as given in Eq. (2). Using an order 25 Fourier series as truth is sufficient for this case as it captures the vast majority of the SRP effects and is thus realistically different from the the simplified models used for estimation from Section 2. Note that because the SRP models that are used for estimation are already simplified compared to the truth model, using a more complicated BRDF to create the truth data would have very little effect on the results shown here. As discussed previously, the effect of the Earth's shadow is ignored here for simplicity. Inclusion of the shadow will change the true trajectories used in the simulations, however the relative filter performance with the different SRP models shouldn't be significantly impacted by this simplification as they would all be affected at the same level.

All of the estimation in the following sections was carried out with a batch square-root information filter (SRIF) with no process noise. The gravity model is assumed to be perfectly known by the filter so that no gravity coefficients are estimated. The SRP model used in the filter is varied by case, as detailed in the following sections. The measurement model is a 3-dimensional position measurement. Noise at a level of 1σ of 5 m in each direction is added to these 3D position measurements. No a priori knowledge is assumed. The measurements are ordered with the ECI frame in which they are produced, so that observation 1 corresponds to the $\hat{\mathbf{X}}_{ECI}$, observation 2 corresponds to the $\hat{\mathbf{Y}}_{ECI}$, and observation 3 corresponds to the $\hat{\mathbf{Z}}_{ECI}$.

Clearly the position measurements at the given accuracy are not a realistic data type for debris objects. The purpose of this paper is to explore the effects of using different force models to estimate catalog objects' orbits, independent of the specific data type. With the optimistic data used in this study, one should expect any reasonable representation of the dynamics will be able to fit the orbit as there is significant information available. On the other hand, if a model does not work in this case, its ability to work in an operational environment must be questioned.

In Section **??** the main problems that arise for estimation when the dynamics are mis-modeled were outlined. In order to clearly determine if these problems are arising and to compare various test models, the following four key metrics are defined. The first two are familiar, and are simply the 3D RMS values of the ECI position and velocity errors over the data arc. These give a direct sense of how well the orbit is fit while data is available. The third metric is the largest single axis position error during the propagation span normalized by the filter's uncertainty for that position. This is written mathematically as

$$\max\left\{\frac{|X_{true}(t)-X_{est}(t)|}{\sigma_X(t)},\frac{|Y_{true}(t)-Y_{est}(t)|}{\sigma_Y(t)},\frac{|Z_{true}(t)-Z_{est}(t)|}{\sigma_Z(t)}\right\}\forall t\in\text{propagation span} \tag{14}$$

If this metric is larger than 3, it is shows that the filter covariance is not realistically bounding the estimation errors. Only the position is used for the third metric because the prediction error, in terms of position, gives a sense for how difficult it will be to locate the object for future measurements and to associate those observations with the previously fit orbit. The fourth metric is the 3D RMS post-fit residual scaled by the measurement noise. Since there are three measurements, this is the RSS of the post-fit residuals in each direction scaled by the RSS of the measurement noise in all three directions. There are no bad or outlier measurements added in these simulations, so this number should be around 1 if the data is being fit to the level of noise.

3.1 Upper Stage in Geosynchronous Transfer Orbit

In the first example, a discarded upper stage in a GTO is examined. This is a common type of debris due to the fact that these spent upper stages typically have lifetimes of nearly 25 years. These uncontrolled objects cross the orbits of many active satellites, especially in low Earth orbit, so it is crucial to have accurate knowledge of their states in order to perform useful conjunction analysis.

The model used for this study is pictured in Fig. 1. This model is sized to roughly represent the upper stage of an Ariane V launch vehicle. Note that only the major features are included here - the model is basically a cylinder with an engine bell. The average $A/m = 0.0055$ m^2/kg, and the optical properties are $\rho = 0.9$ and $s = 0.05$, which represents the white painted surface. The mass is 4540 kg, which is approximately the dry mass of an Ariane V upper stage. Note that the principal axes of inertia are those shown in Fig. 1, with $I_{zz} > I_{yy} > I_{xx}$, where are slightly perturbed from those of a solid cylinder.

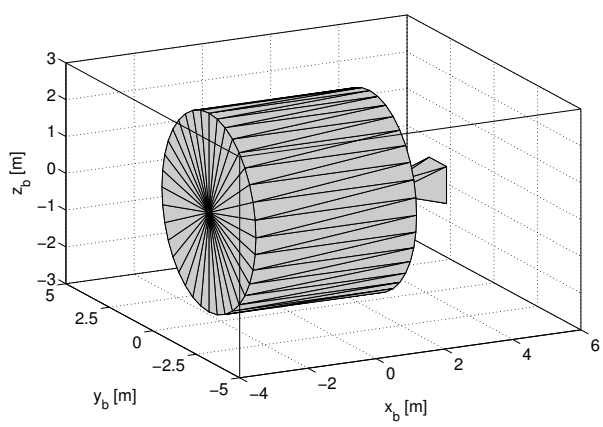

Figure 1: Upper stage shape model used for this study.

In the following sections, the dynamics of the upper stage in the GTO orbit, and the SRP perturbations that act on the vehicle, are analyzed. Then the performance of several different SRP models is compared for estimation and prediction of the upper stage state.

3.1.1 Upper Stage Dynamics

The upper stage is placed in a GTO with an initial apogee at GEO altitude, and an initial perigee altitude of 250 km, with an inclination of 6°. The node is also at apogee, and the line of apses is initially aligned with the Earth-Sun direction, which is the $\hat{\mathbf{X}}_{ECI}$ direction. The simulation begins with the upper stage at apogee.

The upper stage is spinning at a constant rate of 1 revolution per hour about the $\hat{\mathbf{z}}_b$ axis, which is aligned with the orbit normal direction. This is expected to be a possible steady state situation for empty upper stage vehicles since this is the minimum energy configuration. No torques are modeled in this simulation, so that the upper stage spins at a constant rate throughout and the spin axis is fixed in inertial space even as the orbit evolves over time so that at the end of the simulation the spin axis and orbit normals are no longer parallel. This means that this model falls under the classification of the inertially fixed uniform rotator, discussed in Section 2.3.

Based on the orbit geometry and spin state described above, the Sun moves through a full revolution in longitude every hour, while the latitude slowly drifts due to the motion of the Earth around the Sun. At this point in the Earth's orbit, which starts at the vernal equinox, the latitude rate is nearly constant. The SRP forces produced based on this motion with the order 25 Fourier model in the Sun relative frame are shown in Fig. 2. The forces are shown in the Sun relative frame to make clear the differences from the cannonball model, which would only show up as the average force in the $\hat{\mathbf{U}}$ direction, which is pictured as a dotted line in Fig. 2. The motion of the Earth about the Sun can cause appreciable differences in the SRP perturbation; in this case, as the Earth moves the magnitude of the oscillations in the $\hat{\mathbf{U}}$ direction shrinks while those in the $\hat{\mathbf{W}}$ direction grow. Not only are the periodic terms completely missed by the cannonball model, but there are also non-zero average forces in the $\hat{\mathbf{V}}$ and $\hat{\mathbf{W}}$ directions that are completely ignored by that model.

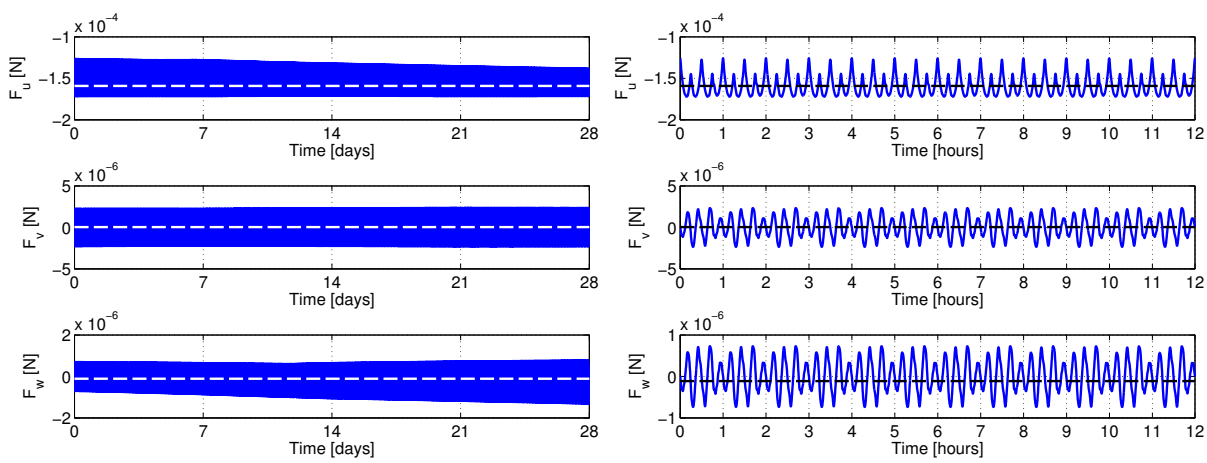

Figure 2: The true SRP force for the 28 days (left) and a zoomed view on the first 12 hours (right), along with the average values (dotted lines).

The true SRP model is generated through the force maps shown in Fig. 3. Note that these maps are generated for the body-fixed reference frame, and so do not directly correspond to the UVW axes shown in Fig. 2 due to the fact that the body is spinning. These force maps could be computed with any given SRP model, and give a 3D SRP force for any location of the Sun in the body-fixed frame. In this simulation the Sun starts in the body equatorial plane, and sweeps through all longitudes as while slowly decreasing the latitude toward the body's south pole. It is interesting to note that the effect of the self-shadowing of the body can be seen in these maps. Consider, for example, the two roughly circular features around $\lambda_s = \pm 90°$ in the F_y plot. As the Sun moves away from the engine bell toward the front of the vehicle ($\lambda_s = 180°$), the engine bell becomes shadowed by the body of the vehicle, causing those circles to be distorted. When the Sun moves toward the back of the vehicle where the engine bell resides, there is no self shadowing, and so the feature stays circular on the map.

Intuitively, for an object like the upper stage considered here, the effect of solar radiation pressure is expected to be small due to the fact that the area-to-mass ratio of this object is fairly small. Furthermore, this reasoning can easily be extended to think that modeling the SRP perturbation with the cannonball model would be sufficient to capture the vast majority of the effects on the orbit. In fact, the perturbation from SRP should certainly not be ignored, and

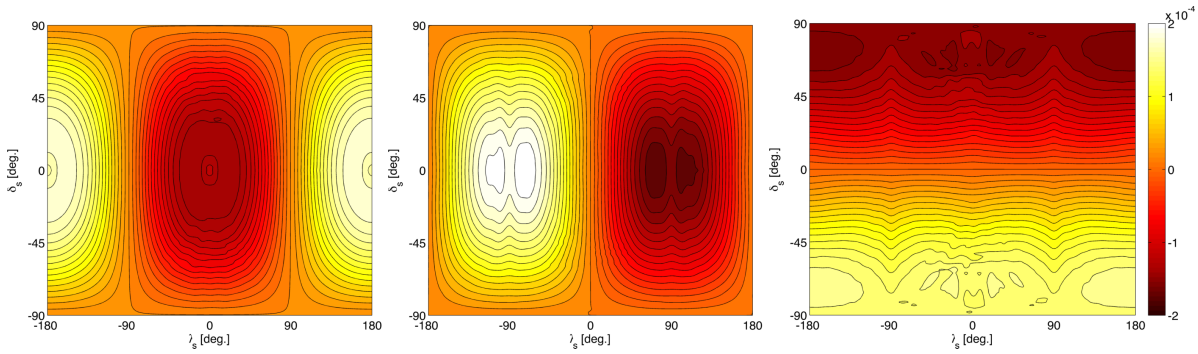

Figure 3: Contour plots of the Fourier model force (N) in the body frame ($\hat{\mathbf{x}}_b$ left, $\hat{\mathbf{y}}_b$ center, $\hat{\mathbf{z}}_b$ right).

furthermore the difference in effects between the cannonball model and the true SRP perturbation generated from Fig. 3 is significant.

This is illustrated by comparing two 5-day propagation of the upper stage, one using the cannonball model for SRP, and the other using the true SRP model represented in Fig. 3. The differences between these two propagations is illustrated in Fig. 4. These results show that over only 5 days, significant errors appear when using the cannonball model. These errors are growing with time, so the idea that the perturbative effects from components of the SRP force perpendicular to the $\hat{\mathbf{u}}$ direction will average out is not true. Thus a fundamental weakness of the cannonball model is that it will not generate the correct secular evolution that will occur with a more realistic model [5, 4].

Note that in the case shown in Fig. 4, the cannonball model used was ``perfect'' in that it was the true average of the SRP force in the $-\hat{\mathbf{u}}$ direction. If the value used for the cannonball model was incorrect, for example if the TLE ballistic coefficient was used here as is sometimes done in practice, these errors would be even larger since the SRP and drag perturbations are fundamentally independent processes.

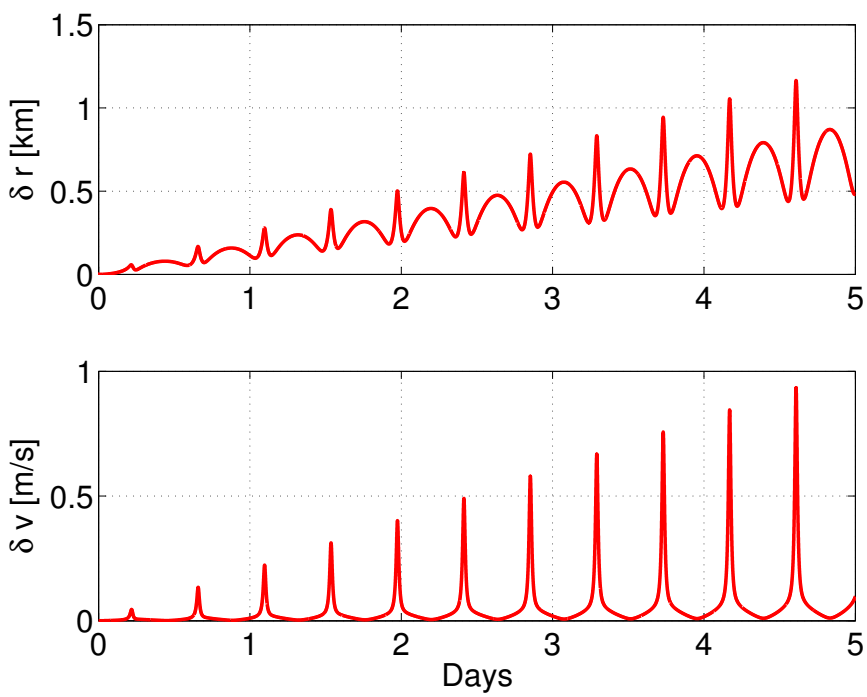

Figure 4: Orbit propagation error magnitudes (position above, velocity below) over 5 days.

3.1.2 Upper Stage Estimation

In the previous section, a realistic SRP model for a spinning upper stage in GTO was shown to have significant acceleration components that are not well represented by the cannonball model, and furthermore that these differences cause significant errors in propagation of the upper stage orbit. In this section, three different simplified models for representing the SRP acceleration in the filter dynamics used for orbit determination are examined. The three models used are the cannonball model, the 3-constant model from Section 2.2, and an order 1 Fourier series model with the inertially fixed uniform rotator assumptions (i.e. the spin axis and rate are known a priori) from Section 2.3.

In these examples, the dynamics presented in the previous section are used as the true trajectory, and are used to generate the measurement data. Measurements are created at 10 second intervals for the first 5 days of the true trajectory. The resulting state and covariance estimates are then propagated out to 28 days from the initial epoch so the prediction accuracy can be assessed. Clearly this is a data rich scenario that should be easily fit if the dynamic model is reasonably accurate.

First the performance of the cannonball model is examined, which is the baseline model used in many (or most) orbit determination solutions. The SRP acceleration for this model was given in Eq. (7). There is only one coefficient to be estimated with this model, which is a scale factor on the total SRP acceleration. The a priori value for the coefficient is 1 as the cannonball force has been set as the average of the true model in the $\hat{\mathbf{u}}$ direction, as shown by the dotted line in Fig. 2.

The results from the fit are summarized in Figs. 5 and 6. In Fig. 5, the post-fit residuals indicate that the fit using the cannonball model over the 5 days of data is not very accurate. In this simulation, the $\hat{\mathbf{X}}_{ECI}$ direction is nearly aligned with $\hat{\mathbf{u}}$ during the data arc, and it is clear that the cannonball model fits the data in this direction the best in that the residuals, while certainly large compared to the noise and containing distinctive structure, are at least spread so that they appear to have a zero mean. In the other two directions, the fit is worse as the residuals are growing with time. Since this is a simulation, the state errors with respect to the known truth trajectory can be computed - these are shown in Fig. 6. The classic issues with dynamic model errors are clearly illustrated. The state errors grow outside of the 3σ covariance bounds during the fit, and badly violate the bounds during the propagated trajectory. Furthermore, as seen in the residuals, the errors contain both periodic and secular components so that the fit will continue to drift from the truth as time goes on. It is interesting to note that the state errors at the epoch are very small, and the estimated cannonball scale factor turns out to be $C_R = 0.996$, which is basically what was given as an input. Thus, the bottom line is that the cannonball model is incapable of fitting this data.

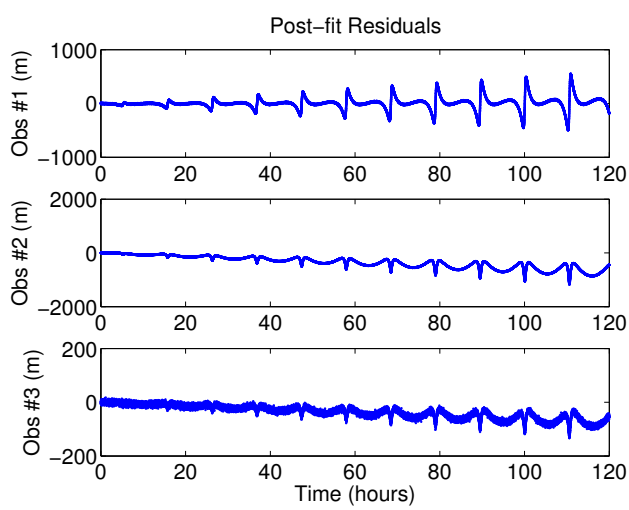

Figure 5: Post-fit residuals using the cannonball model.

The post-fit residuals and state errors for the 3-constant case are in Figs 7 and 8, respectively. It is immediately clear that the fit is much better in this case. The post-fit residuals appear to be zero mean white noise, and their magnitude is in line with the 5 m 1σ noise added to the measurements. Furthermore, the state errors appear to be contained within the 3σ covariance bounds both during the data arc, and for the full propagation period out to 28 days. Simply comparing the scale of Fig. 8 to that in Fig. 6, it appears that the fit is improved by a factor of 5-10 in the orbit plane directions,

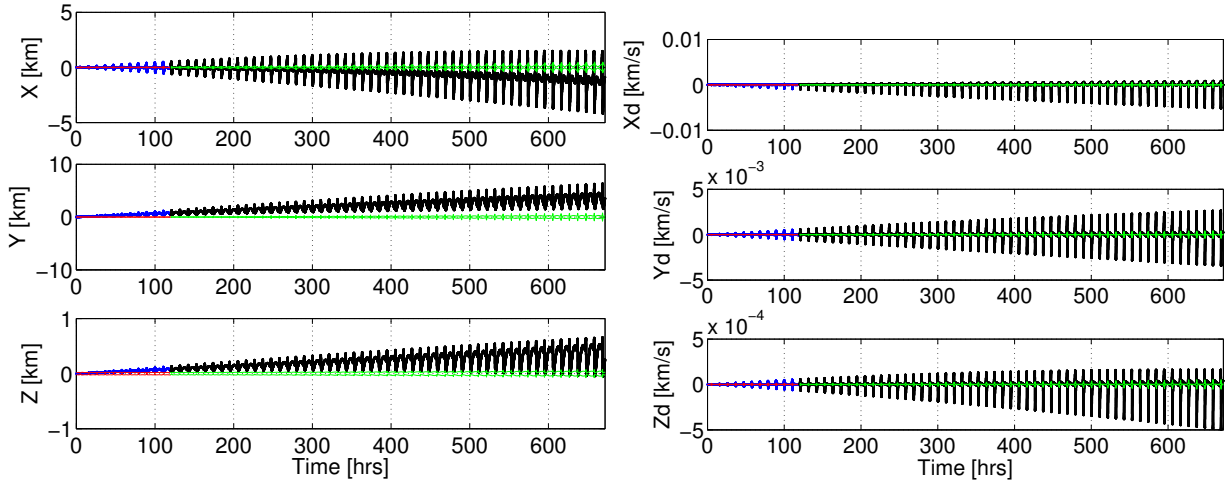

Figure 6: Position and velocity state errors (blue during data arc, black during propagation) and 3σ covariance bounds (red during data arc, green during propagation) using the cannonball model.

and still a factor of 2 improvement out-of-plane.

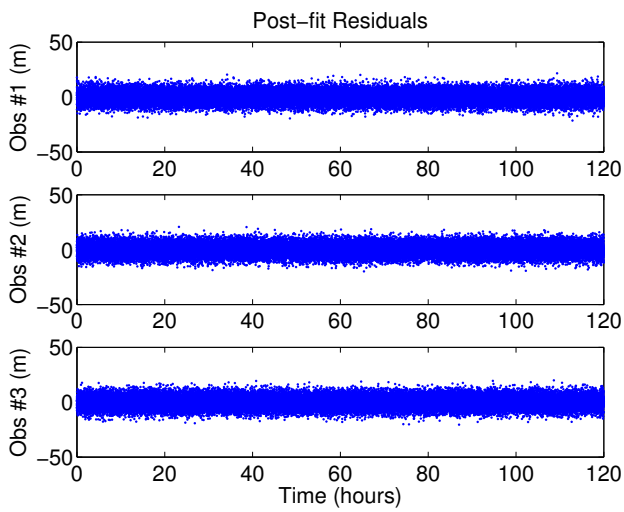

Figure 7: Post-fit residuals using the 3 constant model.

Finally, the post-fit residuals and state errors for the Fourier model case are given in Figs. 9 and 10. The results are interesting in that the post-fit residuals appear to be fit well for the first 36 hours, but then some structure creeps in signifying some mis-modeling in the dynamics. The source of this mis-modeling is the fact that the amplitude of the periodic component of the SRP acceleration changes as the solar latitude drifts, as was seen in Fig. 2. The filter does a good job of fitting the periodic amplitude during the 5 days of data, but as it drifts over time during the end of the data arc and onto the prediction phase, a periodic error appears in the residuals. Regardless of these errors, it appears that this model produces state errors of very similar magnitude to the 3-constant model.

To make more concrete comparisons of the performance of the three models, the four metrics outlined in Section 3 are evaluated. These results are given in Table 1. As mentioned above, these metrics make clear the fact that cannonball model can not fit this set of data. The 3-constant model fits the data slightly better than the Fourier model over the 5 day arc, but the Fourier model ends up providing more accurate propagation of the estimate despite the worse fit to the data. Closer comparison of the final propagated positions for the 3-constant model and the Fourier model are shown in Fig. 11. This shows the power of including the first order terms from the Fourier series - although the fit was not

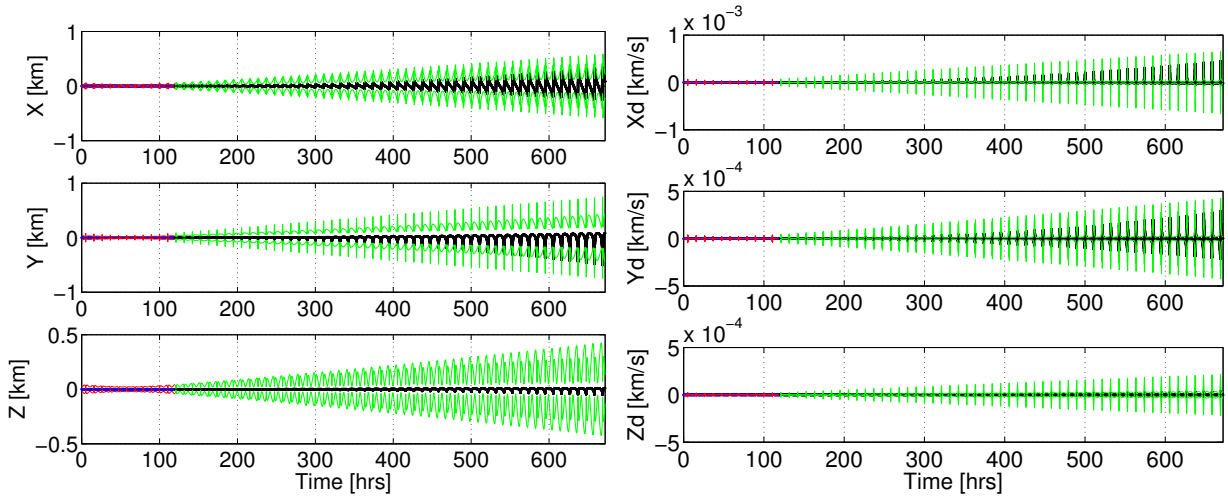

Figure 8: Position and velocity state errors (blue during data arc, black during propagation) and 3σ covariance bounds (red during data arc, green during propagation) using the 3 constant model.

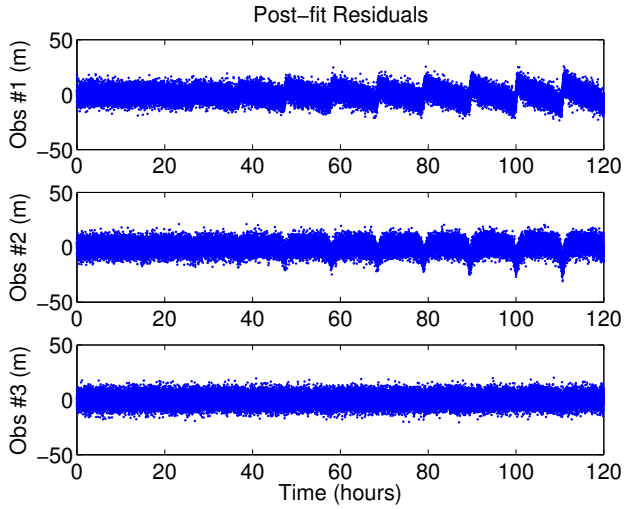

Figure 9: Post-fit residuals using the Fourier model.

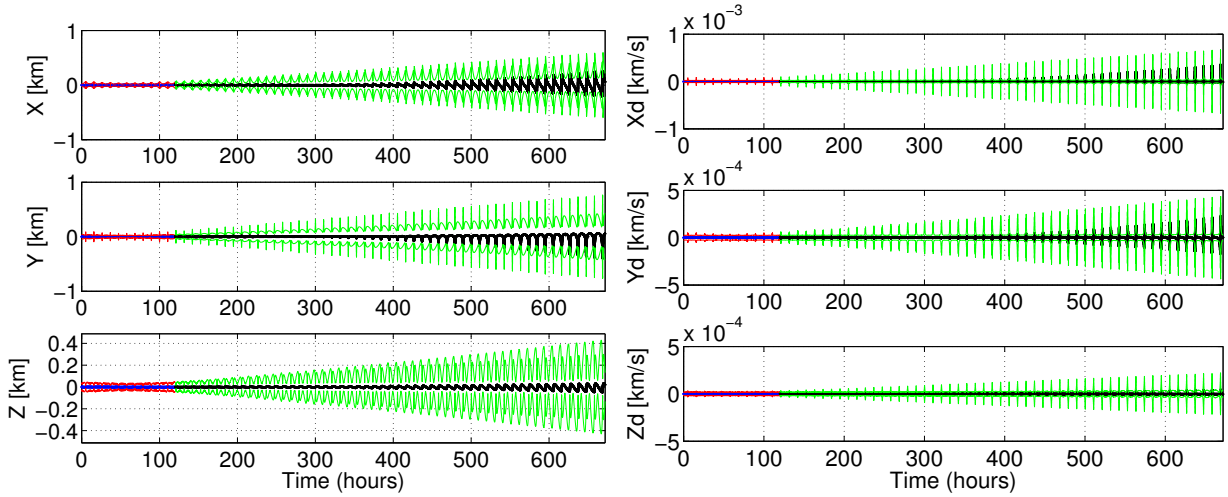

Figure 10: Position and velocity state errors (blue during data arc, black during propagation) and 3σ covariance bounds (red during data arc, green during propagation) using the Fourier model.

quite as good, the propagation actually holds up slightly better than the 3-constant model. Note that the covariance for the $\hat{\mathbf{Z}}_{ECI}$ direction are outside the scale of these axes. The periodic spikes in the uncertainty and errors correspond to passage through perigee where small orbit phase differences cause large changes in cartesian location. This time period, however, is generally the most crucial portion of the orbit to have accurate predictions since that is where the danger for impact with active satellites and other debris is highest.

It is important to point out that fitting the Fourier model requires more information to start and more dense measurements. In this case the model is provided with the true spin rate and spin axis, presumably determined previously from lightcurve data. In reality this information would have some, possibly significant, errors that would impact the performance of the fit. Furthermore in this intentionally simplified case, there is a measurement roughly every degree of rotation of the body which gives good observability for fitting the Fourier coefficients. In fact, given this much data and a known spin state one could likely fit more accurate models for the SRP acceleration, however since this is unlikely to occur in practice, it is deferred here.

Table 1: Upper stage fit metrics for the three different SRP models tested.

Case	3D Pos. [m]	3D Vel. [m/s]	Prop. [σ]	Resids. [σ]
Cannonball	437	0.115	70.55	50.51
3 Constant	0.156	6.45e-5	2.06	0.998
Fourier	4.21	1.97e-3	1.59	1.11

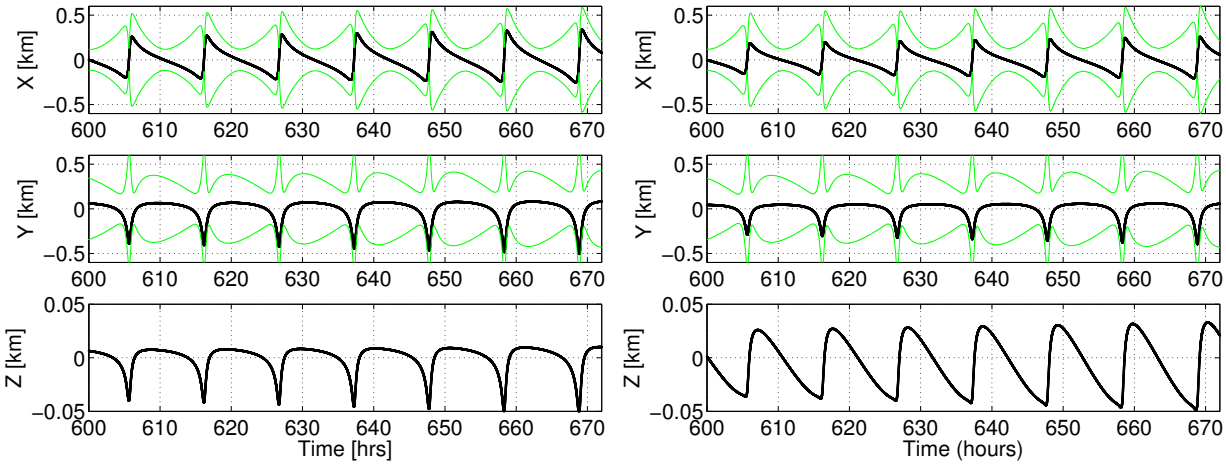

Figure 11: Comparison of the propagation position errors and 3σ covariance envelopes around 28 days from epoch for the 3 constant model (left) and Fourier model (right).

3.2 High Area-to-Mass-Ratio Debris in Geosynchronous Orbit

A large population of HAMR objects have been observed in the GEO region [2], and much of this population is thought to be made up of pieces of multi-layered insulation (MLI) made of materials such as Mylar[21]. By their very nature, HAMR objects are very susceptible to large perturbations from SRP as has been shown in [8, 12, 20, 6, 21]. In this example the effects of using various SRP models for orbit determination of a piece of Mylar MLI are studied. The shape model used for this study is shown in Fig. 12. It is approximately a 10 cm square, but it is wrinkled by perturbing the various facets out of the initial plane of the sheet. The $A/m = 10\ \mathrm{m}^2/\mathrm{kg}$ for this object. The surface is assumed to have a reflectivity of $\rho = 0.4$, most of which is specular with $s = 0.9$. The dynamics for the particular case analyzed are presented in the next section, followed by an analysis of the performance of the various SRP models tested for estimation of this objects orbit.

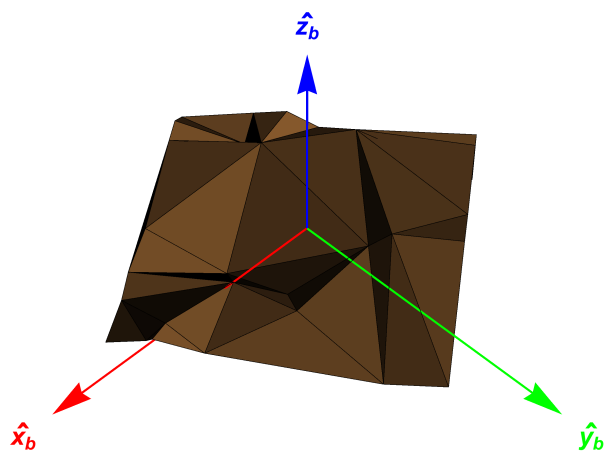

Figure 12: Wrinkled plate shape model used for this study.

3.2.1 High Area-to-Mass-Ratio Dynamics

The case of a HAMR piece of mylar debris is more complicated than a larger body like the upper stage considered previously for two main reasons. First, the AMR is much larger so that the perturbation from SRP perturbs the orbit much more quickly and dramatically. Second, the attitude is uncontrolled and is highly coupled with the orbital motion - for a given attitude with respect to the Sun the body will feel a force and a torque due to SRP, which will then drive both the attitude and orbit evolution. Therefore the simulation used for this scenario includes the full 6-DOF dynamics of the HAMR object including the SRP forces and torques. The true moments of inertia are calculated for the wrinkled shape and are used to determine the attitude evolution.

In this scenario, the HAMR object is placed in a GEO orbit with a random attitude and zero initial angular velocity. The attitude motion and resulting SRP force is illustrated in Figs. 13 - 15. These figures show, respectively, the Sun position in the body frame through its latitude and longitude and the body's angular velocity, contour plots of the true SRP model force in the body-fixed frame vs. the Sun's position, and the time history of the SRP force over the three day propagation.

The behavior of the HAMR attitude is interesting in this case - although it initially starts with no angular velocity, this rapidly changes due to the SRP torques acting on the object that has very small moments of inertia. The solar angles in Fig. 13 show that the body is effectively tumbling to start, however after a few hours the body settles into a rotation state where it wobbles about the $\hat{\mathbf{z}}_b$ and $\hat{\mathbf{y}}_b$ axes (the maximum and intermediate moments of inertia, respectively), and is accelerating around the minimum moment of inertia axis. As the angular velocity increases about $\hat{\mathbf{x}}_b$, the amplitude of λ_s and δ_s shrinks.

Fig. 15 also shows the average SRP force in each direction over time, which is determined from the λ_s and δ_s force maps shown in Fig. 14. Note that the average values in the $\hat{\mathbf{v}}$ and $\hat{\mathbf{w}}$ *are not zero* as they would be with the cannonball model. It is also interesting to note that there seems to be a more significant drift in the mean value and amplitude of the oscillations in this case compared to the upper stage case discussed previously.

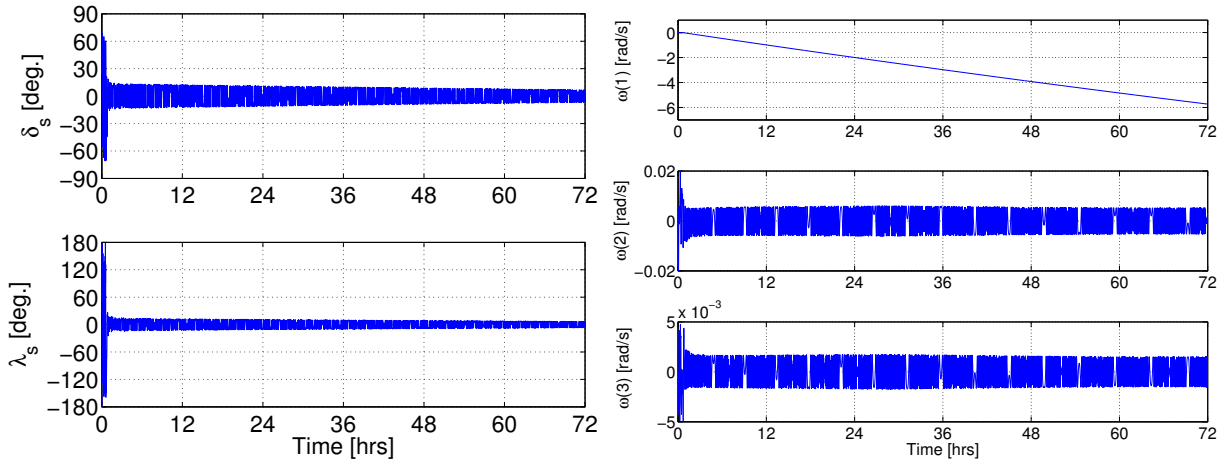

Figure 13: Solar latitude and longitude in the debris body frame (left) and the debris angular velocities (right).

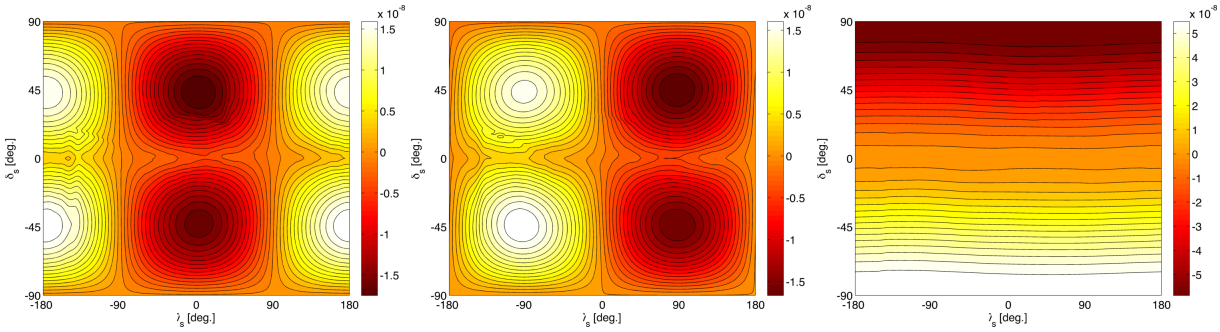

Figure 14: Contour plots of the Fourier model force (N) in the body frame ($\hat{\mathbf{x}}_b$ left, $\hat{\mathbf{y}}_b$ center, $\hat{\mathbf{z}}_b$ right) as a function of the Sun's position.

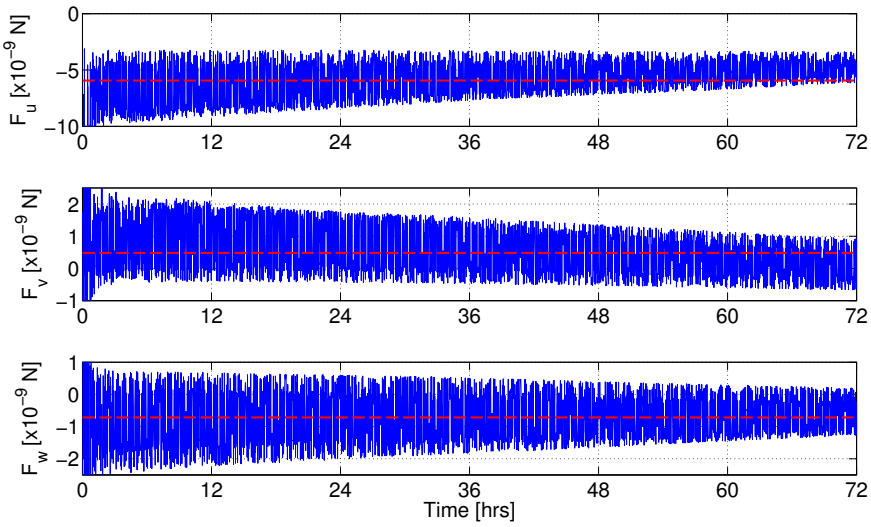

Figure 15: Truth SRP force computed from the order 25 Fourier model (blue) and the time averaged values (red) in the Sun relative frame.

The difference between this case and the upper stage case is significant, as is illustrated in Fig. 16. Here, the HAMR object was propagated for only 3 *days* and the magnitude of the position errors between the true SRP case and the cannonball model case grow to over 1000 km! Furthermore we again see a secular growth in the errors which the cannonball model is not capturing. This implies that much more care must be taken with SRP modeling for HAMR objects to achieve accurate propagation.

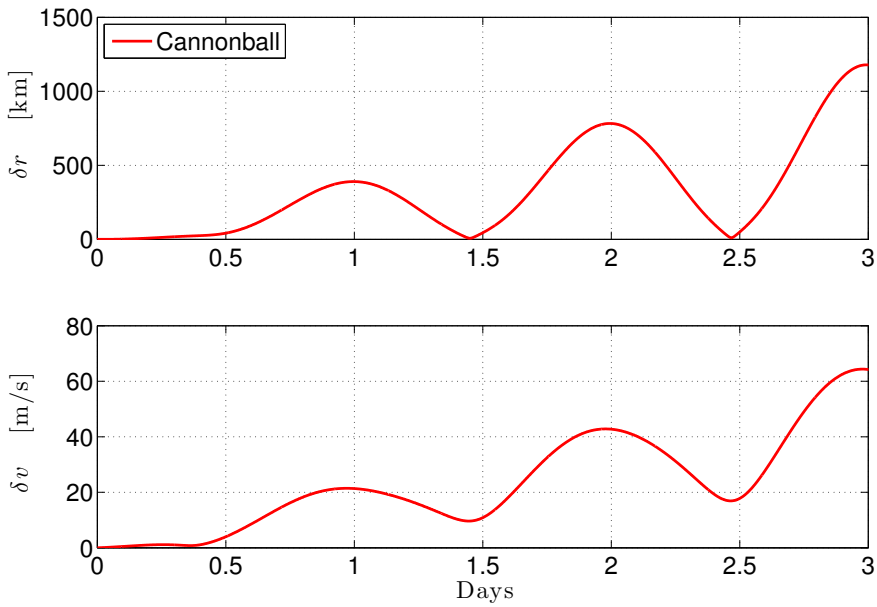

Figure 16: Orbit propagation magnitude errors (position errors on top, velocity below) over 3 days

3.2.2 High Area-to-Mass-Ratio Estimation

In this section, three different SRP models are tested. The first is the cannonball model, the second is the 3-constant model in the $\hat{\mathbf{u}}$, $\hat{\mathbf{v}}$, and $\hat{\mathbf{w}}$ directions, and the third case is a first order Fourier series model based on the orbit frequency, as discussed in Section 2.4. The performance of each of these models are investigated and compared for processing various arcs of data at 1 minute frequency. Initially, the performance of each model for processing an 8 hour arc of data is shown, similar to the upper stage results in Section 3.1.

The fit obtained by using the cannonball model for 8 hours of data is shown in Fig. 17. Here a typical example of how poorly the cannonball model fits HAMR tracking data is seen. Given the amount of data processed, the filter believes that it has a lot of information and so the covariances are very small. However, due to the fact that the filter is using an improper model for the SRP, the state errors drift well outside of the 3σ bounds within a few hours. Since the observations in this case are simply the position components, this also shows that the observation residuals are orders of magnitude higher than the measurement noise.

Given these results, it is not surprising that the propagation of this estimated state does not stay very close to the true state, as shown in Fig. 18. Furthermore the propagated covariance is completely unrealistic and barely captures any of the data.

The same set of data is processed with the 3-constant case, and the results are shown in Fig. 19. Although the model has only two additional estimated parameters, the performance is vastly improved. Each component of the state is fit to better than 100 m for the entire 8 hour arc, and every point is well inside the 3σ bounds. The 3-constant model does not capture the true SRP dynamics as there is a non-noise signal present (recall that the position errors are equivalent to observation residuals). However, the residuals are less than 100m throughout, which compared to the multiple kilometer residuals obtained with the cannonball model, is a significant improvement.

Fig. 20 shows the propagation of the estimated state and covariance. Again, due to the fact that this is still a simplified SRP model, the state errors grow with time. Compared to the cannonball case, however, the performance has been greatly improved. The state errors are about an order of magnitude less than the cannonball case. Most

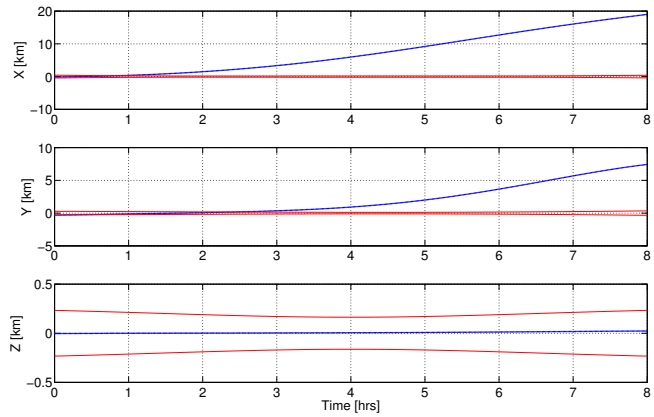

Figure 17: Position errors of the cannonball fit of an 8 hour arc of data.

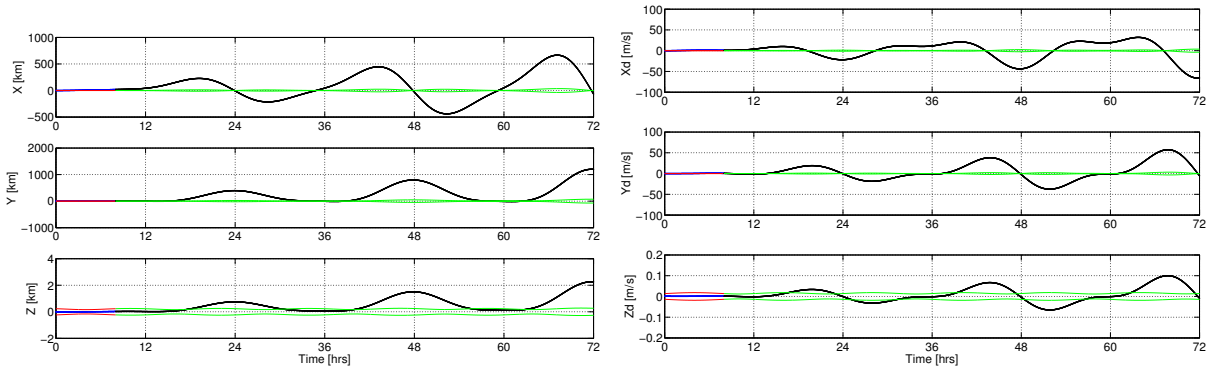

Figure 18: Position and velocity errors and covariance from 8 hour cannonball fit propagated to 72 hours.

importantly, however, the 3σ covariance bounds are more realistic in this case. To be clear, the state errors still go outside of the covariance envelope, but at least in this case they are following roughly the same pattern as the covariance bounds and are near to the bounds. In other words, this case captures at least *some* correct information about the propagated system.

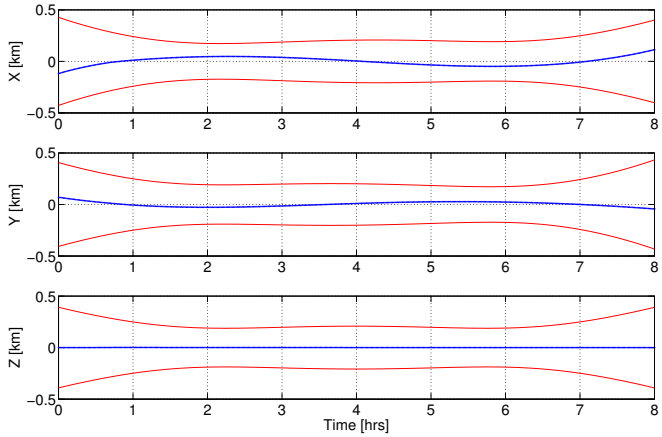

Figure 19: Position errors of the 3 constant fit of an 8 hour arc of data.

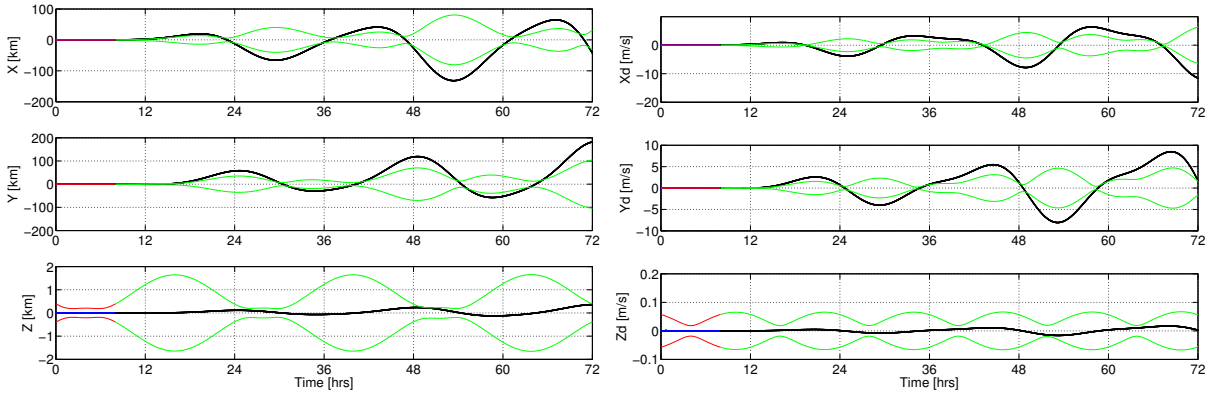

Figure 20: Position and velocity errors and covariances from 8 hour 3 constant fit propagated to 72 hours.

Finally, we compare the performance of the first order Fourier model. As with the previous two cases, the position errors during the fit are shown in Fig. 21 and the propagated states are shown in Fig. 22. As with the 3 constant case, the Fourier model fits the data over the 8 hour are extremely well, and much better than the cannonball model. Interestingly the propagation with the Fourier model is more accurate than the 3 constant model - position errors grow to around 30 km in X and Y, and less than 1 km in Z, and velocity errors grow to around 1.5 m/s in X and Y, and to 0.05 m/s in Z. The tradeoff, as is clear in Fig. 22, is that the covariance grows much larger in this case because the same information is spread over 6 extra estimated parameters, so the covariance isn't made as small.

These three cases can be compared more directly through use of the four metrics, given for these cases in Table 2. The cannonball case clearly illustrates three of the four problems with using the incorrect SRP model that were discussed earlier. First, the estimate is basically wrong. Second, this causes the propagation to be wildly inaccurate. Third, the covariance bounds are inappropriately small, and when propagated do not bound the actual position of the object in any way. The second case of estimating the 3-constant SRP force greatly improves all of these issues, but the model is still simplified enough that they do not disappear. The third case of estimating the Fourier model outperforms the other two in all three aspects, although as discussed above the propagation metric is a little misleading because the covariance is much larger for the Fourier estimation. Regardless, this clearly shows the massive performance

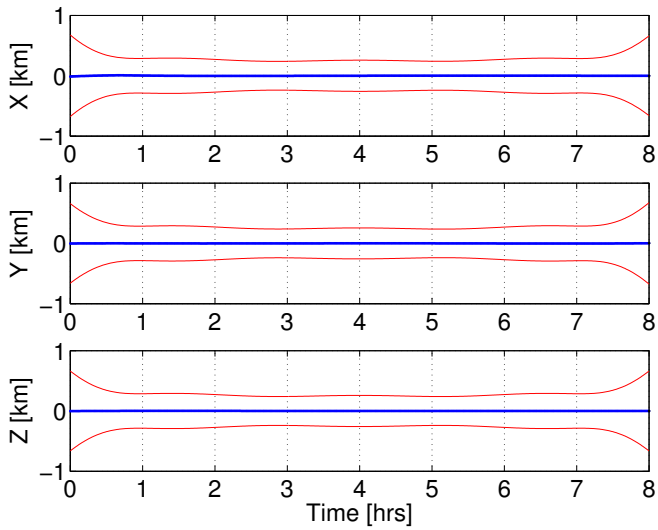

Figure 21: Position errors of the Fourier fit of an 8 hour arc of data.

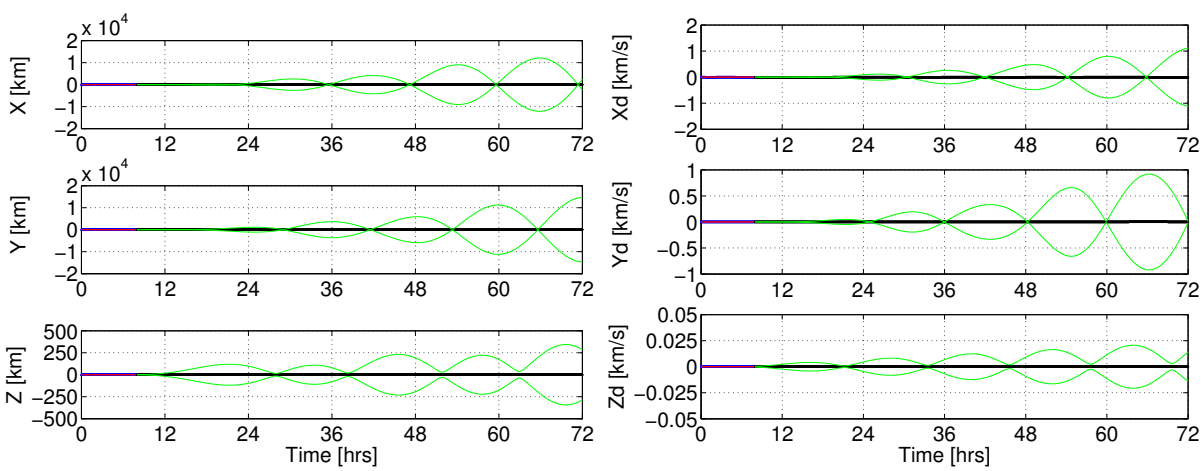

Figure 22: Position and velocity errors and covariances from 8 hour Fourier fit propagated to 72 hours.

improvements in precise orbit determination, prediction, and uncertainty propagation made possible by using a more appropriate SRP model.

Table 2: HAMR fit metrics for three different SRP models with 8 hours of data propagated to 72 hours.

Case	3D Pos. [m]	3D Vel. [m/s]	Prop. [σ]	Resids. [σ]
Cannonball	9964	0.795	143.2	115.1
3 Constant	47.6	0.022	6.24	5.63
Fourier	2.92	0.0032	0.180	1.01

The analysis of the performance of these three models can be extended by looking at a range of fits over various arc lengths of data. Above, the results for an 8 hour arc for each model are shown. In Fig. 23, the 3D position error RMS for each of the models over arc lengths of 1-72 hours are seen. In each arc, there are continuous measurements at 1 minute intervals as before. For all arc lengths processed, the 3-constant SRP model outperforms the cannonball model by about 2 orders of magnitude, and the Fourier model outperforms the 3-constant model.

Fig. 24 shows the post-fit residuals for each model, compared to the pre-fit residuals which are roughly the same for all models since they are mainly due to the erroneous initial conditions. Again, the 3-constant SRP and Fourier models clearly do a much better job of fitting the data for all arc lengths than the cannonball model. It is interesting to point out, however, that for the X and Y directions (where most of the SRP perturbations occur in this simulation) even the 3-constant model can only fit arcs of less than about 6 hours down to the measurement noise. The Fourier model improves on this, fitting over 24 hour arcs down to the noise. Longer arcs contain clear non-noise signals similar to those seen in the example above in Fig. 19.

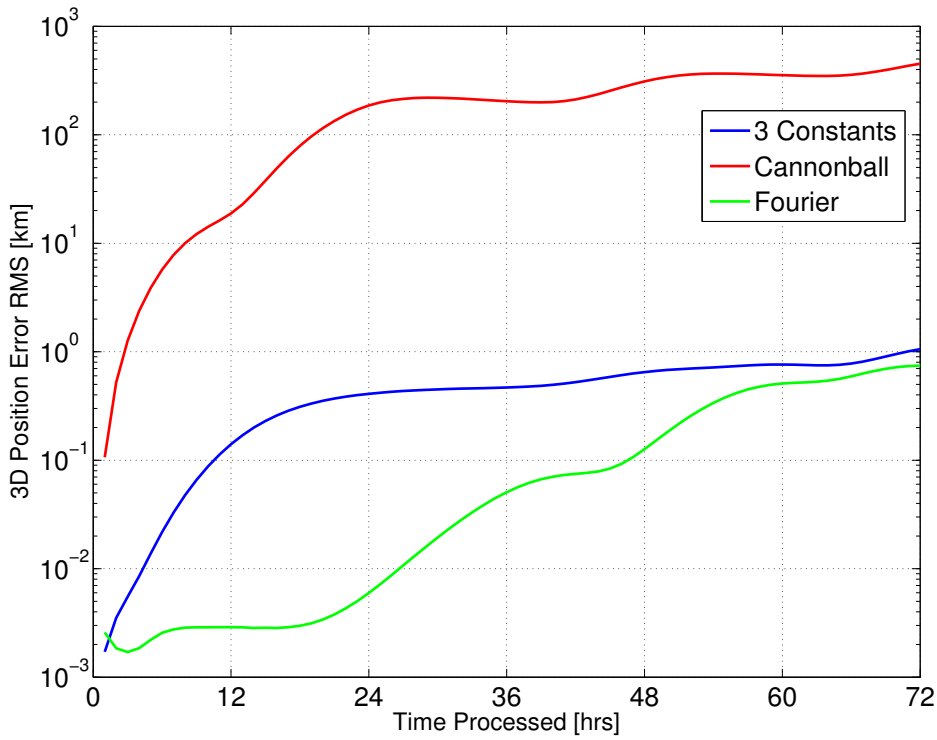

Figure 23: 3D position RMS values for the cannonball, the 3 constant, and the Fourier models for processing arcs of data ranging from 1 to 72 hours.

The final point from the toy model discussion in Section **??** was that a bad force model can prevent the filter from fitting the data. This phenomenon is occurring with the cannonball model, but not with the other two models. The easiest way to see this clearly is to run the filter with the true position and velocity initial conditions so that any improvement in the residuals is purely due to adjusting the SRP model. The residuals for this test are shown in Fig.

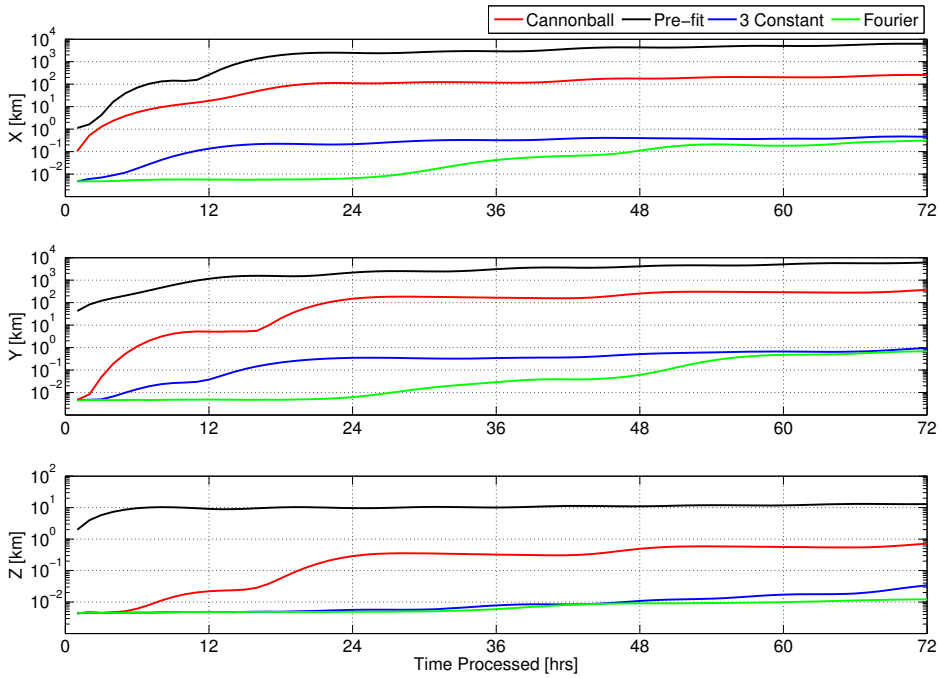

Figure 24: Observation residual RMS values for the cannonball, the 3 constant, and the Fourier models for processing arcs of data ranging from 1 to 72 hours.

25. Note that the Fourier model is initialized differently so that its residuals for this case are different than the other two. For all arcs longer than 2 or 3 hours, *the cannonball model does not improve the residuals.* This is the definition of a filter not fitting the data. In some cases, the filter actually starts diverging and makes the residuals worse. This does not happen at all for the 3-constant or Fourier models for any arc up to 72 hours, thus providing confidence that either can serve as a much better baseline SRP model for HAMR debris than the cannonball model.

The previous examples clearly demonstrated that the cannonball model has difficulty fitting a dense arc of tracking data. However, it might seem intuitive that a simple 1 parameter model like the cannonball model would be preferable for fitting sparser data. To show that this is not the case, the same data set is used, but now only 3 segments of 5 observations are fit (each observation separated by approximately 30 seconds) with a varying amount of time between 2 minute segments. This measurement cadence is illustrated in Fig. 26. As with the previous case, the residuals and the position error RMS values are shown in Figs. 27 - 28.

The results of this test are much the same as the previous test - the 3-constant and Fourier models outperform the cannonball model for all scenarios, with the Fourier model generally performing the best. There is an interesting issue happening for this particular test where the orbit becomes less observable around multiples of 12 hour data gap. This makes sense, as the object is in roughly the same location for all observations so there is minimal information in the second and third segments. Impressively, the Fourier model isn't susceptible to this issue until the data gap reaches 4 days.

4 Conclusion

This paper explicitly illustrates the fundamental issues with using the cannonball model to represent the solar radiation pressure (SRP) perturbation on Earth orbiting objects, and shows how these shortcomings limit the ability to track orbiting objects. The problems associated with the cannonball model can be alleviated by allowing the SRP perturbation to be 3-dimensional, which requires only two extra parameters to be estimated compared to the cannonball model. This is a small cost to improve tracking accuracy by orders of magnitude. Therefore, the recommendation is that the 3-constant model be adapted as the standard model to represent SRP in all cases. The formulation presented in this paper also allows the 3-constant model to be seamlessly expanded into an arbitrary order Fourier series model for

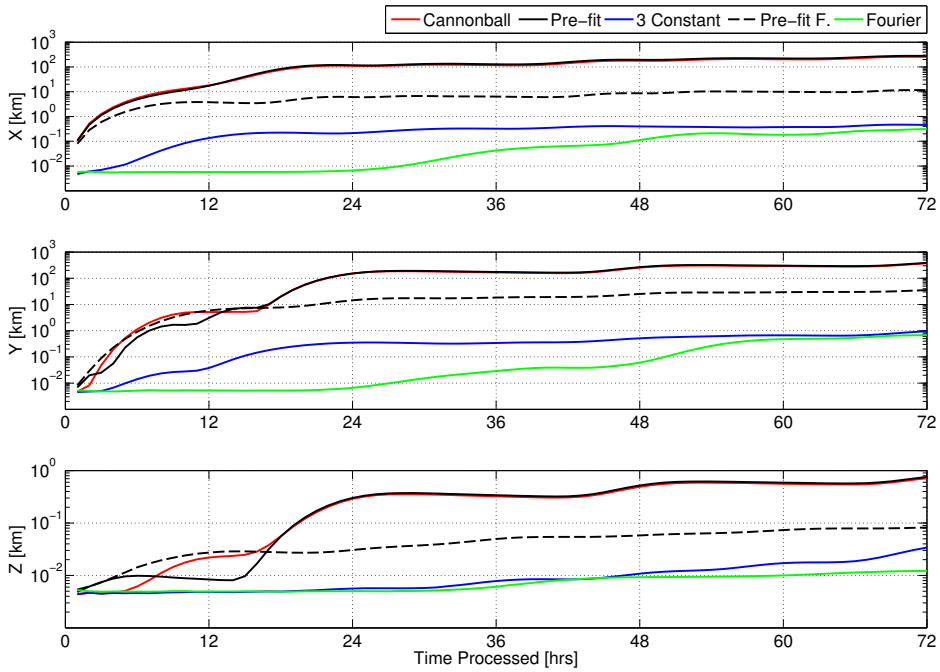

Figure 25: Observation residual RMS values for the cannonball, the 3 constant, and the Fourier models for processing arcs of data ranging from 1 to 72 hours with perfect initial conditions.

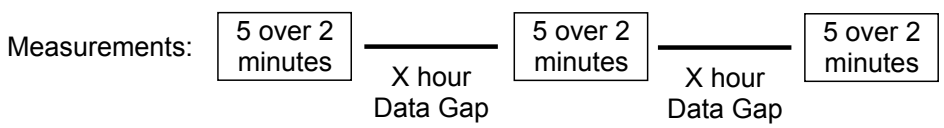

Figure 26: Measurement cadence for sparse data test.

precise orbit determination for those objects where this is appropriate.

In particular, the results presented in this paper show that the cannonball model is not a good representation of the true SRP force acting on an object, especially for high area-to-mass ratio (HAMR) objects. Returning to the basics of estimation theory, it is well established that dynamic modeling errors in a filter ensure that the filter will perform poorly. Although the estimation scenarios here were admittedly simplified, they established that there are fundamental problems with the current system that uses the cannonball model. An improved SRP model, however, could greatly improve catalog maintenance issues over the status quo. An accurate force model allows for precise orbit determination with realistic covariance bounds, and most importantly allows these estimates to be propagated such that the covariance envelope realistically contains the object in the future. This is a necessity for proper track correlation and object identification, which both depend on accurate propagation and covariance realism. Furthermore, using a more realistic force model will reduce sensor tasking issues with current tracking networks. Sensing resources are being wasted to track even large objects, such as the upper stage investigated in this paper, because more regular tracking must be used to make up for the fact that the cannonball based predictions are only useful for short periods of time. Similarly, an improved force model allows longer and more dense arcs of data to be used to maintain catalog entries, which will increase the information associated with these entries since old data will not need to be discarded in order to fit the data.

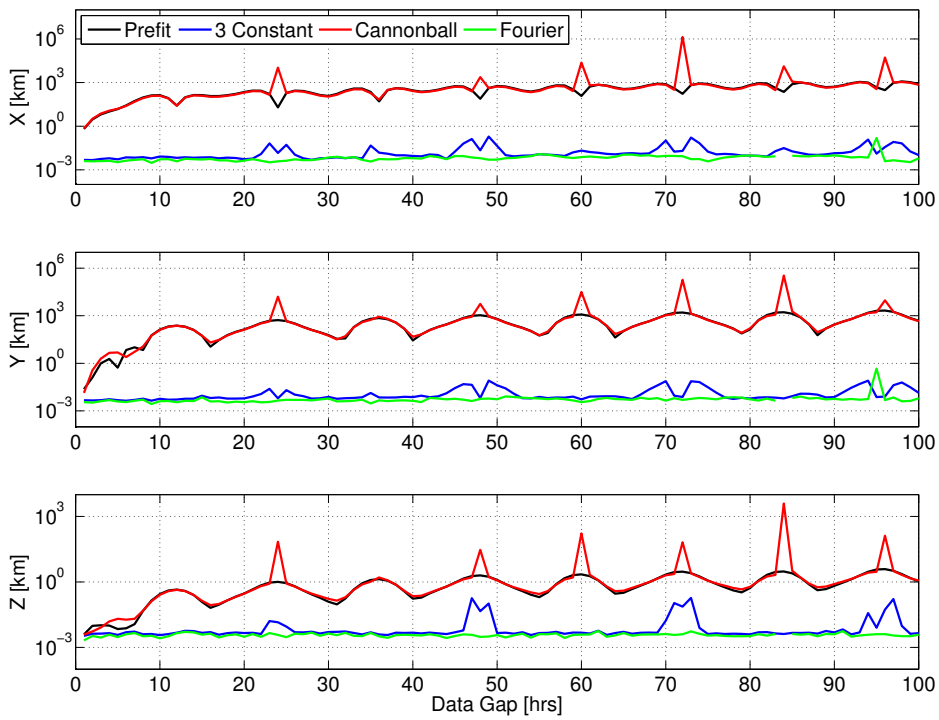

Figure 27: Observation residual RMS values for the cannonball, the 3 constant, and the Fourier models for processing arcs of data with gaps.

Acknowledgments

The authors gratefully acknowledge funding support from AFOSR and the FAA Center Of Excellence for Commercial Space Transportation.

References

[1] Valk, S., Lemaitre, A., and Anselmo, L., ``Analytical and semi-analytical investigations of geosynchronous space debris with high area-to-mass ratios," *Advances in Space Research* Vol. 41, 2008, pp.1077-1090. doi:10.1016/j.asr.2007.10.025

[2] Schildknecht, T., Musci, R., Flohrer, T., ``Properties of the high area-to- mass ratio space debris population at high altitudes", *Advances in Space Research*, Vol. 41, No. 7, 2008, pp. 1039-1045. doi:10.1016/j.asr.2007.01.045

[3] Scheeres, D., ``The dynamical evolution of uniformly rotating asteroids subject to YORP", *Icarus*, Vol. 188, No. 3, 2007, pp. 430-450. doi:10.1016/j.icarus.2006.12.015

[4] McMahon, J. and Scheeres, D.J. ``New Radiation Pressure Force Model for Navigation," *Journal of Guidance, Control and Dynamics*, Vol. 33, No. 5, 2010, pp. 1418-1428. doi:10.2514/1.48434

[5] McMahon, J., and Scheeres, D. J., ``Secular Orbit Variation Due to Solar Radiation Effects: A Detailed Model for BYORP", *Celestial Mechanics and Dynamical Astronomy*, Vol. 106, No. 3, 2010, pp. 261-300. doi:10.1007/s10569-009-9247-9

[6] Anselmo, L., and Pardini, C., ``Long-Term Dynamical Evolution of High Area-to-Mass Ratio Debris Released into High Earth Orbits", *Acta Astronautica*, Vol. 67, No. 1-2, 2010, pp. 204-216. doi:10.1016/j.actaastro.2009.10.017

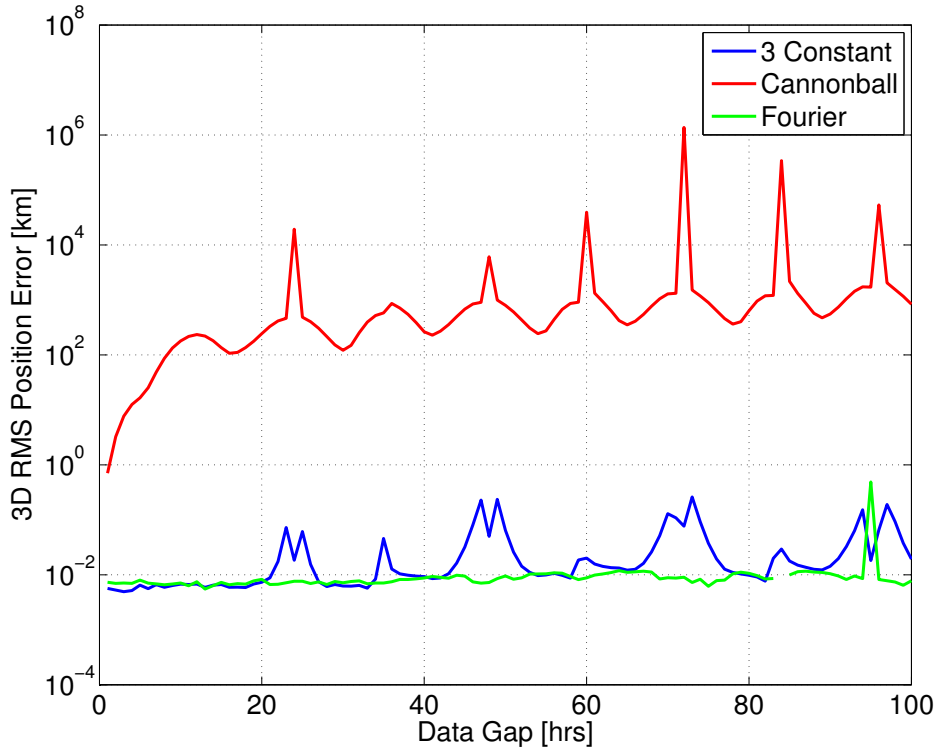

Figure 28: 3D position RMS values for the cannonball, the 3 constant, and the Fourier models for processing arcs of data with gaps.

[7] Scheeres, D. J., Rosengren, A., and McMahon J., ``The Dynamics of High Area-to-Mass Ratio Objects in Earth Orbit: the Effect of Solar Radiation Pressure," Presented at the AAS/AIAA Space Flight Mechanics Meeting, New Orleans, Louisiana, 2011. Paper AAS 11-178

[8] Rosengren, A., and Scheeres, D. J., ``Long-term dynamics of high area-to-mass ratio objects in high-Earth orbit," *Advances in Space Research*, Vol. 52, 2013, pp. 1545-1560. doi:10.1016/j.asr.2013.07.033

[9] Ziebart, M., ``Generalized analytical solar radiation pressure modeling algorithm for spacecraft of complex shape," *Journal of Spacecraft and Rockets*, Vol. 41, No. 5, 2004, pp. 840-848. doi:10.2514/1.13097

[10] Cheng, M., Ries, J., and Tapley, B., ``Assessment of the solar radiation model for grace orbit determination," *Advances in the Astronautical Sciences*, Vol. 129, 2008, pp. 501-510.

[11] Lucchesi, D., ``Reassessment of the error modelling of non-gravitational perturbations on lageos ii and their impact in the lense-thirring determination. part i," *Planetary and Space Science*, Vol. 49, 2001, pp. 447-463. doi:10.1016/S0032-0633(00)00168-9

[12] McMahon J. and Scheeres, D. J., ``Appropriate Modeling of Solar Radiation Pressure Effects on Uncontrolled Orbiting Objects for Accurate Dynamical Predictions," Presented at the AAS/AIAA Space Flight Mechanics Meeting, Charleston, SC, 2012. Paper AAS 12-215

[13] McMahon, J. and Scheeres, D.J. ``General Solar Radiation Pressure Model for Global Positioning System Orbit Determination," *Journal of Guidance, Control and Dynamics*, Vol. 37, No. 1, 2014, pp. 325-330. doi:10.2514/1.61113

[14] Marshall, J. A. and Luthcke S. B., ``Modeling Radiation Forces Acting on Topex/Poseidon for Precision Orbit Determination," *Journal of Spacecraft and Rockets*, Vol. 31, No. 1, January-February 1994, pp. 99-105. doi:10.2514/3.26408

[15] Rim, H. and others, ``Radiation Pressure Modeling for ICESat Precision Orbit Determination," Proceedings of the AIAA/AAS Astrodynamics Specialist Conference and Exhibit, Keystone, CO, August 2006. Paper 2006-6666

[16] Springer, T.A., Beutler, G., and Rothacher, M., ``A New Solar Radiation Pressure Model for GPS Satellites," *GPS Solutions*, Vol. 2, No. 3, 1999, pp 50-62. doi:10.1007/PL00012757

[17] Bar-Sever, Y. E.,``New and Improved Solar Radiation Pressure Models for GPS Satellites Based on Flight Data," Jet Propulsion Laboratory, Pasadena, CA, 1997

[18] Fliegel, H. F. and Gallini, T. E., ``Solar Force Modeling of Block IIR Global Positioning System Satellites," *Journal of Spacecraft and Rockets*, Vol. 33, No. 6, November-December 1996, pp. 863-866. doi:10.2514/3.26851

[19] Committee for the Assessment of the US Air Forces Astrodynamic Standards, et al. *Continuing Kepler's Quest: Assessing Air Force Space Command's Astrodynamics Standards*, National Academies Press, 2012.

[20] McMahon, J., `` Improving Orbit Determination with Non-Cannonball Solar Radiation Pressure Models," Presented at the AAS/AIAA Space Flight Mechanics Meeting, Kauai, HI, 2013. Paper AAS 13-206

[21] Früh, C., Kelecy, T. M., Jah, M. K., ``Coupled orbit-attitude dynamics of high area-to-mass ratio (HAMR) objects: influence of solar radiation pressure, Earth's shadow and the visibility in light curves," *Celestial Mechanics and Dynamical Astronomy*, Vol. 117, 2013, pp. 385-404. doi:10.1007/s10569-013-9516-5

[22] Wetterer, C. J. and others, ``Refining Space Object Radiation Pressure Modeling with Bidirectional Reflectance Distribution Functions," *Journal of Guidance, Control and Dynamics*, Vol. 37, No. 1, 2014, pp. 185-196. doi:10.2514/1.60577

[23] McInnes, Colin R. *Solar sailing: technology, dynamics and mission applications*, Springer, 2004, Chapter 2.

[24] Ashikhmin, M., and Shirley, P., ``An Anisotropic Phong BRDF Model," Journal of Graphics Tools, Vol. 5, No. 2, 2000, pp. 25-32. doi:10.1080/10867651.2000.10487522

[25] Cook, R. L., and Torrance, K. E., ``A Reflectance Model for Computer Graphics," ACM Transactions on Graphics, Vol. 1, No. 1, Jan. 1982, pp. 7-24. doi:10.1145/357290.357293

[26] Schildknecht, T. ``The Search for Space Debris Objects in High-Altitude Orbits." Astronomical Institute, University of Bern, Habilitation treatise, 2003.

[27] Valk, S., et al. ``Global dynamics of high area-to-mass ratios GEO space debris by means of the MEGNO indicator." Advances in Space Research Vol. 43, No. 10, 2009, pp. 1509-1526.

[28] Lemaître, A., N. Delsate, and S. Valk. ``A web of secondary resonances for large A/m geostationary debris." Celestial Mechanics and Dynamical Astronomy, Vol. 104, No. 4, 2009, pp. 383-402.

[29] Früh, C., and T. Schildknecht. ``Variation of the area-to-mass ratio of high area-to-mass ratio space debris objects." Monthly Notices of the Royal Astronomical Society, Vol. 419, No. 4, 2012, pp. 3521-3528.

[30] Hubaux, Ch, and A. Lemaître. ``The impact of Earths shadow on the long-term evolution of space debris." Celestial Mechanics and Dynamical Astronomy, Vol. 116, No. 1, 2013, pp. 79-95.

[31] Tapley, B., Schutz, B., and Born, G.H, *Statistical Orbit Determination*, Academic Press, 2004.

[32] McMahon, J., Scheeres, D., ``Improving Space Object Catalog Maintenance Through Advances in Solar Radiation Pressure Modeling", *Journal of Guidance, Control, and Dynamics*, Vol. 38, No. 8, 2015, pp. 1366-1381. doi:10.2514/1.G000666